Accepted Manuscript

Title: Prediction of contact angle for hydrophobic surface fabricated with micro-machining based on minimum Gibbs free energy

Author: Shi Zhenyu Liu Zhanqiang Song Hao Zhang Xianzhi

Please cite this article as: S. Zhenyu, L. Zhanqiang, S. Hao, Z. Xianzhi, Prediction of contact angle for hydrophobic surface fabricated with micro-machining based on minimum Gibbs free energy, *Applied Surface Science* (2015), http://dx.doi.org/10.1016/j.apsusc.2015.12.199

Prediction of contact angle for hydrophobic surface fabricated with micro-machining based on minimum Gibbs free energy

Shi Zhenyu[a], Liu Zhanqiang[a,*], Song Hao[a], Zhang Xianzhi[b]

[a]*Key Laboratory of High Efficiency and Clean Mechanical Manufacture*

(Shandong University), Ministry of Education, P. R. China)

[b]*School of Mechanical and Automotive Engineering, Kingston University, UK*

*Corresponding author, Telephone: 86-0531-88393206, Fax: 86-531-88392045,

melius@sdu.edu.cn

Abstract: When an interface exists between a liquid and a solid, the angle between the surface of the liquid and the outline of the contact surface is described as the contact angle. The size of the contact angle is the metrics of the hydrophobicity of the surface. The prediction of the contact angle has significant effect on the design of hydrophobic surface and improvement of hydrophobicity. In this paper, a prediction model for contact angle has been proposed based on minimum Gibbs free energy. It considers the effects of unilateral force and area constraints of the droplets. The effect of micro-structural parameters on contact angle has also been investigated. Micro-milling experiments have been conducted to fabricate the hydrophobic surface in order to validate the predictive capability of the contact angle model. Results revealed that the established prediction model could estimate the contact angle of hydrophobic surface. The contact angle could be increased by increasing concave width or reducing convex. The outcome of this research will lead to new methodologies for preparing hydrophobic surfaces with micro-machining technology.
KEYWORDS : Hydrophobic surface, Contact angle, Energy method, Micro-milling

1. Introduction

Surface with directional wetting properties is of significant practical importance in

many fields [1,2], especially for self-cleaning, reduction of condensate retention and drag reduction, etc. The lotus leaves can keep off raindrops and dust due to the micro/nano-morphology of their surfaces, and this phenomenon is referred to as "lotus effect"[3]. The contact angle, as shown in Fig. 1, is the angle at which the liquid-vapor interface meets the solid-liquid interface [4]. A contact angle less than 90º (low contact angle) usually indicates that wetting of the surface is very favorable, and the fluid will spread over a large area of the surface. Contact angles greater than 90º (high contact angle) generally means that wetting of the surface is unfavorable. The fluid will minimize contact with the surface and form a compact liquid droplet. Hydrophobic surfaces with contact angle greater than 150º show almost no contact between the liquid and the surface [5,6].
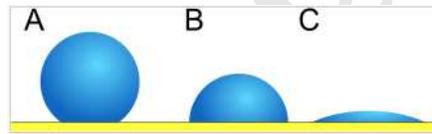

Fig. 1. Wetting of different fluids: A has a large contact angle, B has a common

contact angle and C has a small contact angle

The contact angle was described by Thomas Young for the first time in 1805, which is defined by the mechanical equilibrium of the droplet under the action of three interfacial tensions (Fig. 1) under ideal solid surface [7].

$$\cos\theta = \frac{\gamma_{SV} - \gamma_{SL}}{\gamma_{LV}} \tag{1}$$

γ_{SV}, γ_{SL} and γ_{LV} represent the solid-vapor, solid-liquid and liquid-vapor interfacial tensions respectively, and θ is the contact angle.

Depending on the way a droplet rests on a rough surface, two wetting states, Wenzel and Cassie-Baxter, are generally defined. The Wenzel model assumes that the liquid wets the whole rough substrate, while the Cassie-Baxter model assumes that the droplet partially wets the rough substrate due to the trapped air in the micro-structured surfaces as shown in Fig. 2 [8,9].
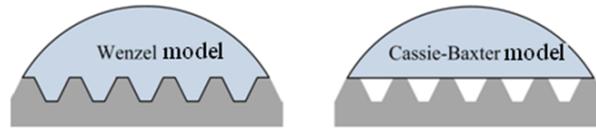
Fig. 2. Wenzel and Cassie-Baxter model

The Wenzel model is defined by Eq.2 for the contact angle on a rough surface:

$$\cos\theta_W = r \times \cos\theta \tag{2}$$

where θ_W is the apparent contact angle which corresponds to the stable equilibrium state; r is the roughness ratio which is defined as the ratio of true area of the solid surface to the apparent area.

The Cassie-Baxter model is defined as shown in Eq. 3.

$$\cos\theta_{CB} = -1 + \left(1 + r_f\cos\theta\right) \times f \tag{3}$$

where r_f is the roughness ratio of the wet surface area, and f represents the fraction of solid surface area wet by the liquid.

It can be seen that when $f=1$ and $r_f = r$, the Cassie-Baxter equations becomes to be the Wenzel equation [10,11]. It can also be seen that under the same Yong contact angle, the contact angle calculated by Wenzel model is less than θ, while the contact angle calculated by Cassie-Baxter is greater than θ. It should be realized that both Wenzel and Cassie-Baxter models all consider the surface roughness can help to increase the hydrophobicity of the surface. However, there is still a lack of investigation on the quantitative dependence relationship of the macroscopically effective contact angle on the micro-structured surface parameters of surface roughness.

Johnson and Dettre [12] proposed that for a hydrophobic surface with sinusoidal structure, when the surface roughness has a low value of surface roughness, the wetting state is Wenzel. When the surface roughness is equal to or higher than a critical value, the wetting mode for a deposited liquid droplet would be Cassie on a surface. Song et al. [13] investigated the static and dynamic hydrophobicities of water droplets on a patterned surface prepared using fluoroalkylsilane with different

molecular chain lengths. Their results imply that the sliding acceleration of water droplets on hydrophobic surfaces is controllable by changing the pattern structure and its chemical composition. At present, most of the research on super hydrophobic properties focuses on the preparation technology of superhydrophobic materials, but there is still a need for further effect to study the wetting behavior of superhydrophobic materials, and fundamental problems such as which parameters are more suitable for judging the superhydrophobicity of a material. The comprehensive understanding of the dynamic contact angle and internal flow pattern of water droplets on micro-structured superhydrophobic surfaces is still insufficient. Therefore, it is still an unresolved issue to determine which model should be employed to calculate the contact angle of a specified micro-structured surface.

Current microfabrication technology permits more controlled experiments where the roughness of the surface can be quantified in terms of the geometric parameters. Established surface micro-structure methods include micro-machining, electro-chemical machining, electrical discharge machining, embossing and laser ablation. Micro-machining entails removal of material from a substrate using a cutting tool and chip removal to leave a desired geometry. The precision of micro-machining can reach micrometer-scale, with nanometer-scale surface finish. Song et al. [14] fabricated partially grooved hydrophobic surfaces and results showed that the apparent contact angle parallel to the grooves is larger than that on smooth surface, while the micro-structures have little effect on contact angle in vertical direction. It can be seen that the anisotropic effect of the micro-structures would be more significant by increasing the fraction of the grooved area. Wan et al. [15] fabricated columnar micro-structure arrays on aluminum alloy substrate by using a high speed precise micro-milling machine. It is found that the columnar micro-structure arrays can effectively improve the hydrophobic properties of aluminum alloy, and the contact angle is improved from 51° up to 115°. However, how the micro-structures affect the wetting models and what are the spreading behavior on different materials surface are not discussed.

This paper aims to establish a contact angle prediction model based on minimum

Gibbs free energy. Then the effects of micro-structured surface parameters on contact angle are investigated. Finally, micro-milling experiments are conducted to fabricate the hydrophobic surface and to validate the predictive capability of the contact angle model.

2. Establishment of contact angle prediction model

2.1 Determination of contact parameters

According to Gibbs free energy [16], a general rule of thumb is that every system seeks to achieve a minimum of free energy. In this paper, by building up the relationship between the Gibbs free energy of droplets on the surface and the contact angle, the contact angle corresponding to the minimum Gibbs free energy is considered to be the stable contact angle. Surface tension is a contractive tendency of the surface of a liquid that allows it to resist an external force. At constant temperature and pressure, surface tension equals to Gibbs free energy per surface area.

$$\sigma = \left. \frac{\partial G}{\partial A} \right|_{T,P,n} \tag{4}$$

where G is Gibbs free energy and A is the area of droplet.

Hence, according to the contact area and surface tension of solid-vapor, solid-liquid and vapor-liquid, the Gibbs free energy for droplets can be obtained. In this research, the droplet is supposed to be two-dimensional pattern. The cross section is dome, and the cross-sectional area keeps constant. Hence, the Gibbs free energy reflected in two dimensional is contact force as shown in Eq. 5

$$F = \gamma_{SL} \times L_{SL} + \gamma_{SV} \times L_{SV} + \gamma_{LV} \times L_{LV} \tag{5}$$

where F is contact force, L_{SL}, L_{SV} and L_{LV} represent the solid-liquid, solid-vapor and liquid-vapor contact length respectively.

In this paper, the droplet partially wets the rough substrate which reflected the hydrophobic phenomenon is investigated (Cassie-Baxter model). There are still two situations for a droplet rest on substrate convex as shown in Fig. 3 either on inside or outside, where Fig.3 (a) shows the droplet rest on outside of the convex and Fig.3 (b)
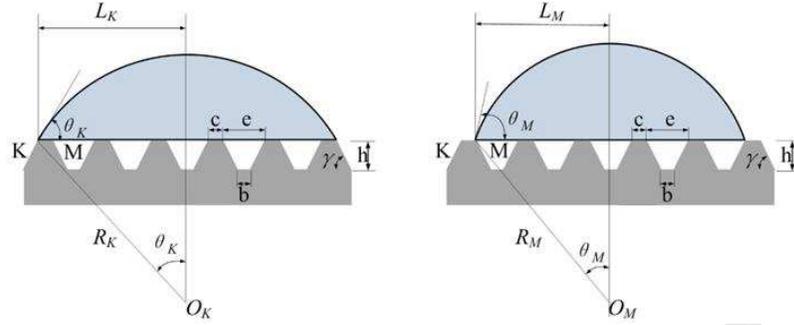
shows the droplet rest on inside of the convex.

Fig. 3. Droplet rest on outside and inside of convex

In Fig. 3, c represents the width of convex and e represents the concave width. h is the height of the convex. b is length of solid-vapor for single micro-structured surface. γ is tilt angle of micro-structured surface.

Table 1 shows the parameters of droplet rests on micro-structured surface.

Table 1 Droplet parameters resting on micro-structured surface

	Droplet rest on outside of convex	Droplet rest on inside of convex
Number of concave n	$\dfrac{2L_K - c}{c + e}$	$\dfrac{2L_M + c}{c + e}$
L_{LV}	$\dfrac{\theta_K L_K}{sin\theta_K} + ne$	$\dfrac{\theta_M L_M}{sin\theta_M} + ne$
L_{SL}	$(n+1)c$	$(n-1)c$
L_{SV}	$n\left(2\dfrac{h}{sin\gamma} + b\right)$	$n\left(2\dfrac{h}{sin\gamma} + b\right)$

2.2 Relationship between contact force and contact angle

Substituting the parameters in Table 1 into Eq. 5, the contact force and the area constraint of droplet can be obtained.

Eq. 6 and Eq. 7 show the contact force and the area constraint for droplet rest on

outside of convex.

$$F_K = \gamma_{SL} \times (n+1)c + \gamma_{SV} \times n\left(2\frac{h}{\sin\gamma} + b\right) + \gamma_{LV} \times \left(\frac{\theta_K L_K}{\sin\theta_K} + ne\right) \tag{6}$$

$$\theta_K \frac{L_K^2}{\sin^2\theta_K} - L_K^2 \cot\theta_K = S \tag{7}$$

Divided by γ_{LV} on both sides, Eq. 6 can be expressed as shown in Eq. 8, which represents the relationship between contact energy and contact angle:

$$\frac{F_K}{\gamma_{LV}} = \frac{\gamma_{SL}}{\gamma_{LV}} \times (n+1)c + \frac{\gamma_{SV}}{\gamma_{LV}} \times n\left(2\frac{h}{\sin\gamma} + b\right) + \frac{\theta_K L_K}{\sin\theta_K} + ne \tag{8}$$

For the situation that droplet rests on outside of convex, the number of concave covered by droplet n can be expressed as Eq. 9:

$$n = \frac{2L_K - c}{c+e} \tag{9}$$

Putting Eq. 9 into Eq. 8, Eq. 8 can be expressed as Eq. 10 or Eq. 11:

$$\frac{F_K}{\gamma_{LV}} = \frac{\gamma_{SL}}{\gamma_{LV}} \times \left(\frac{2L_K - c}{c+e} + 1\right)c + \frac{\gamma_{SV}}{\gamma_{LV}} \times \frac{2L_K - c}{c+e}\left(2\frac{h}{\sin\gamma} + b\right) + \left(\frac{\theta_K L_K}{\sin\theta_K} + \frac{2L_K - c}{c+e}e\right)$$

$$\tag{10}$$

or:

$$\frac{F_K}{\gamma_{LV}} = \left(\frac{\theta_K}{\sin\theta_K} + \frac{2e}{c+e} + \frac{\gamma_{SL}}{\gamma_{LV}}\frac{2c}{c+e} + \frac{\gamma_{SV}}{\gamma_{LV}}\frac{2\left(2\frac{h}{\sin\gamma}+b\right)}{c+e}\right)L_K + \left(\frac{\gamma_{SV}}{\gamma_{LV}}\frac{ec}{c+e} - \frac{ec}{c+e} - \frac{\gamma_{SV}}{\gamma_{LV}}\frac{c}{c+e}\left(2\frac{h}{\sin\gamma}+b\right)\right)$$

$$\tag{11}$$

Eq.7 can also be changed into Eq. 12:

$$L_K^2 = \sin^2\theta_K \frac{S}{\theta_K - \cos\theta_K \sin\theta_K} \tag{12}$$

And L_K can be expressed as:

$$L_K = sin\theta_K \sqrt{\frac{S}{\theta_K - cos\theta_K sin\theta_K}} \tag{13}$$

Putting Eq.13 into Eq. 11, it can be changed into Eq. 14:

$$\frac{F_K}{\gamma_{LV}} = \frac{\theta_K}{sin\theta_K} + \frac{2e}{c+e} + \frac{\gamma_{SL}}{\gamma_{LV}}\frac{2c}{c+e} + \frac{\gamma_{SV}}{\gamma_{LV}}\frac{2\left(2\frac{h}{sin\gamma}+b\right)}{c+e}\left(sin\theta_K\sqrt{\frac{S}{\theta_K - cos\theta_K sin\theta_K}}\right) + \frac{\gamma_{SV}}{\gamma_{LV}}\frac{ec}{c+e} - \frac{ec}{c+e} - \frac{\gamma_{SV}}{\gamma_{LV}}$$

$$\tag{14}$$

For $cos\theta = (\gamma_{SV}-\gamma_{SL})/\gamma_{LV}$, Eq. 14 can be simplified as shown in Eq. 15:

$$\frac{F_K}{\gamma_{LV}} = \frac{\theta_K}{sin\theta_K} + \frac{2e-2ccos\theta}{c+e}\left(\sqrt{\frac{S}{\frac{\theta_K}{sin^2\theta_K} - cot\theta_K}}\right) + \frac{cos\theta(ec-1)}{c+e} \tag{15}$$

For droplet resting inside of convex, the contact force and the area constraint can be represented as Eq. 16 and Eq. 17 respectively:

$$F_M = \gamma_{SL} \times (n-1)c + \gamma_{SV} \times n\left(2\frac{h}{sin\gamma}+b\right) + \gamma_{LV} \times \left(\frac{\theta_M L_M}{sin\theta_M} + ne\right) \tag{16}$$

$$\theta_M \frac{L_M{}^2}{sin^2\theta_M} - L_M{}^2 cot\theta_M = S \tag{17}$$

According to the same procedure, the relationship between contact energy and contact angle for droplet resting inside of convex can be expressed as Eq. 18:

$$\frac{F_M}{\gamma_{LV}} = \frac{\theta_M}{sin\theta_M} + \frac{2e-2ccos\theta}{c+e}\left(\sqrt{\frac{S}{\frac{\theta_M}{sin^2\theta_M} - cot\theta_M}}\right) + \frac{cos\theta(ec+1)}{c+e} \tag{18}$$

Comparing Eq. 15 and Eq. 18, it can be found that under the same structural parameters, the contact energy for droplet resting outside of convex is always less. It indicates that the status for droplet resting outside of convex is more stable.

Stepping technique was adopted to derivate the graph which demonstrates the relationship between the contact energy and the contact angle. At first, suppose the droplet resting on an ideal substrate surface, inside of the convex and the initial contact angle is 180º with the calculated contact energy σ_1. Then, extend the droplet to

the outside of the convex, by applying geometric analysis to get the contact angle σ_2. Repeat the process to extend the droplet on both sides to calculate the corresponding contact energy σ_3. Using this method, σ_4, σ_5, etc. can be gained successively. Finally, the graph for the relationship between contact energy and contact angle can be drawn. According to graph, the contact angle corresponding to the minimum contact force is the estimate contact angle.

Fig. 4 shows the relationship between the contact energy and the contact angle when $c=50\mu m$, $e=100\mu m$ and $S=2\times10^6\mu m^2$.

Fig. 4. Fitting energy curve between F_M/γ_{LV} and contact angle

From Fig. 4, it can be seen that the contact angle corresponding to the minimum contact energy is 150°. It indicates that under this surface pattern, the stable contact angle is estimated to be 150°.

According to Eq. 15 and Eq.18, the impact factor $K=(2e-2ccos\theta)/(c+e)$ affects the shape and lowest point of Fig. 4, while $cos\theta(ce\pm1)/(c+e)$ can only affect the vertical position of Fig. 4.

The fitting curve for the contact energy and the contact angle under different values for K is illustrated in Fig. 5.
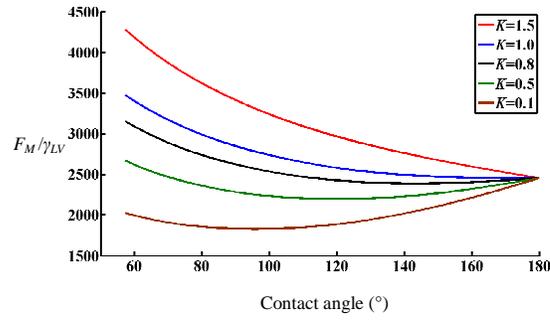
Fig. 5. Fitting energy curve between F_M/γ_{LV} and contact angle under different K value

From Fig. 5, it can be seen that with decrease of K, the contact energy becomes lower and so does of the stable contact angle. When $K=1$, the estimate contact angle is 150º; when $K=0.5$, the estimate contact angle is 120º; and when $K=0.1$, the estimate contact angle is 90º. It is clear that it needs a larger K to increase the actual contact angle. According to the expression of K, increasing concave width or reducing convex width can help to increase the value of K which in turn increases the contact angle. According to the expression of K, it also can be seen that the materials with larger Yong contact angle, have a relative larger K value. That means under the same micro-structure, the materials with hydrophobic substrate can have higher growth and upside potential of contact angle compared to that of materials with hydrophilic substrate.

3. Experimental verification

3.1 Preparation of experiments

Experimental work has been carried out to verification the estimated contact angle during micro-milling process. Workpiece material was selected to be PMMA for its characteristics of good transparency, chemical stability and easy to process. In order to investigate the effect of material on the performance of hydrophobic, further experiments have been conducted and with the workpiece material of Ti6Al4V for its characteristics of excellent mechanical properties and wide application in the fields of Biomedicine. The workpieces were machined on KERN 2522 micro-milling center as

shown in Fig. 6 with solid cemented carbide micro-milling cutter. The experiments were carried out under a constant feed per tooth 0.02μm/Z, a radial depth of cut 75μm, an axial depth of cut 100μm and spindle rotation speed 10000r/min.
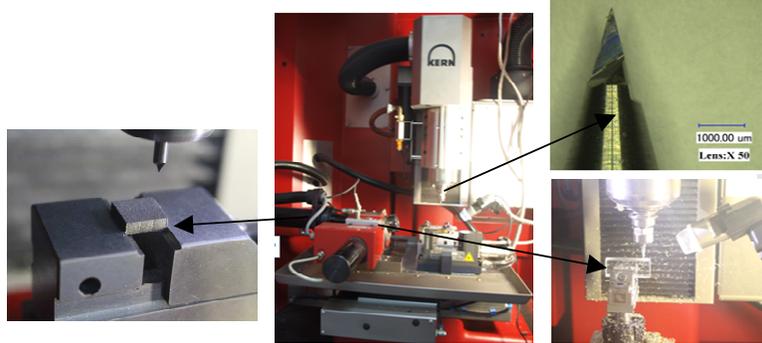

Fig. 6. Micro-milling experiments setup

During the cutting process, both the concave width e and the height of the convex h were fixed to be 100μm. The width of convex varies between experiments to investigate the effect of micro-structured surface on surface hydrophobic properties which means the tilt angle for micro-structured surface γ is 90º. The convex width were selected to be 50μm, 75μm, 100μm, 125μm, 150μm，200μm respectively.

3.2 Test of hydrophobic performance

The images of the obtained micro-structured surface under optical microscope in Fig. 7 show that the machined surfaces have regular grating patterns.

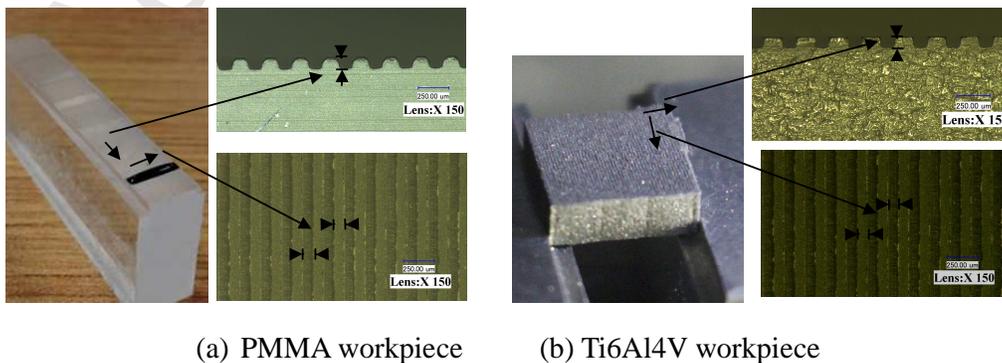(a) PMMA workpiece   (b) Ti6Al4V workpiece

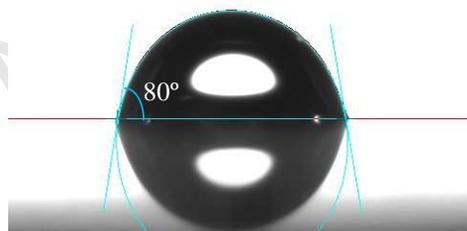Fig. 7. Obtained micro-structured surface under optical microscope

Fig. 7 (a) shows the obtained micro-structured surface for PMMA, and Fig. 7 (b) shows the obtained micro-structured surface for Ti6Al4V.

Fig. 8 shows the optical contact angle measuring instrument. The static and dynamic contact angle can be obtained through the instrument. The drop shape can also be analyzed according to Pendant Drop method.
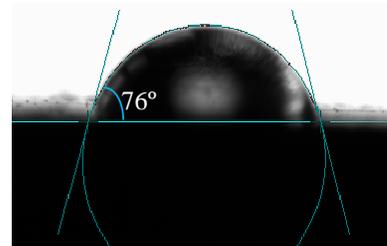

Fig. 8. Optical contact angle measuring instrument

The test liquid used is deionized water with density ρ=996kg/m^3, surface tension σ=0.07275N/m, viscosity μ=0.001kg/ms, and the droplet volume is 2μl. Before the cutting experiments, un-machined sample PMMA and Ti6Al4V was test, and the average contact angle was test to be 80º and 76 º, as shown in Fig. 9.

(a) Contact angle for PMMA   (b) Contact angle for Ti6Al4V

Fig. 9. Contact angle for un-machined sample

The micro-grating pattern can make the droplet anisotropy, which means the

droplet resting on micro-structured surface with strip state instead of sphere. Hence, it is necessary to measure the contact angle in two directions [17]. Fig. 10 (a) shows the observation direction vertical to the grating pattern, and Fig. 10 (b) shows the observation direction parallel to the grating pattern.
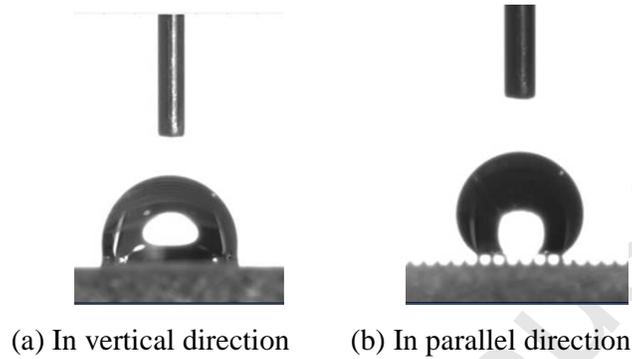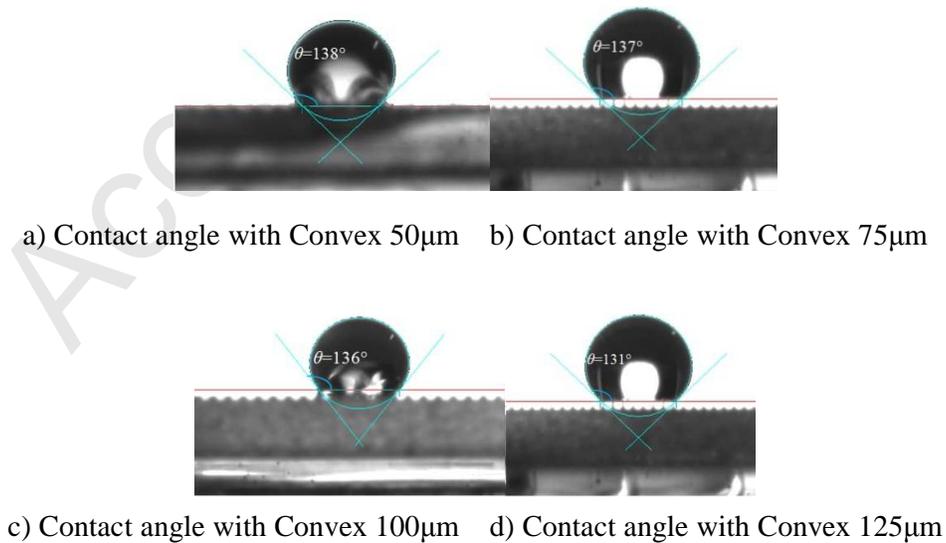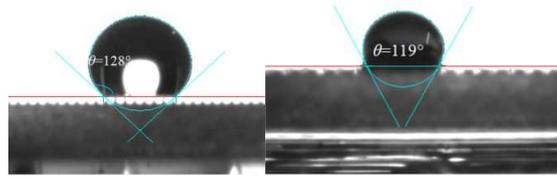

(a) In vertical direction   (b) In parallel direction

Fig. 10. Measuring of contact angles from different direction

4. Results and discussion

Fig. 11 shows the obtained contact angles for six different PMMA samples with convex width 50μm, 75μm, 100μm, 125μm, 150μm，200μm respectively from parallel direction.

a) Contact angle with Convex 50μm   b) Contact angle with Convex 75μm

c) Contact angle with Convex 100μm   d) Contact angle with Convex 125μm

e) Contact angle with Convex 150μm f) Contact angle with Convex 200μm

Fig. 11. Contact angles with different convex from parallel direction

The contact angle for un-machined PMMA workpiece was tested to be 80º. According to Eq. 2 and Eq. 3, the theoretical contact angles for Wenzel and Cassie-Baxter model can be calculated as shown in Table 2. Table 2 also shows the obtained contact angles for six different PMMA samples with different convex widths using different methods.

Table 2 Contact angle obtained through different methods for PMMA

Width of convex/μm	Wenzel model θ_W/°	Cassie-Baxter model θ_{CB}/°	Prediction model θ/°	Vertical direction θ/° ($\pm$SE)	Parallel direction θ/° ($\pm$SE)
50	63	128	150	109$\pm$2[a]	138$\pm$4[b]
75	68	120	138	105$\pm$3[a]	137$\pm$3[b]
100	70	115	134	102$\pm$4[a]	136$\pm$5[b]
125	71	111	130	100$\pm$3[a]	131$\pm$6[b]
150	72	107	126	98$\pm$4[a]	128$\pm$4[b]
200	73	103	122	81$\pm$3[a]	119$\pm$6[b]

SE represent standard error from the mean value of 6 replicates, different letters represent significant differences (p≤0.05).

Table 3 shows the contact angle obtained through different methods for Ti6Al4V workpiece.

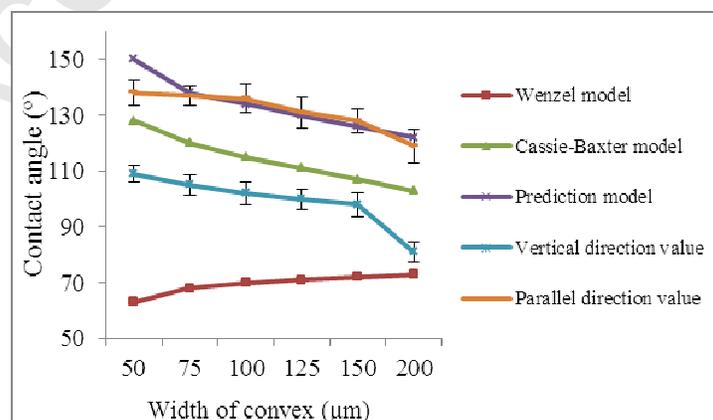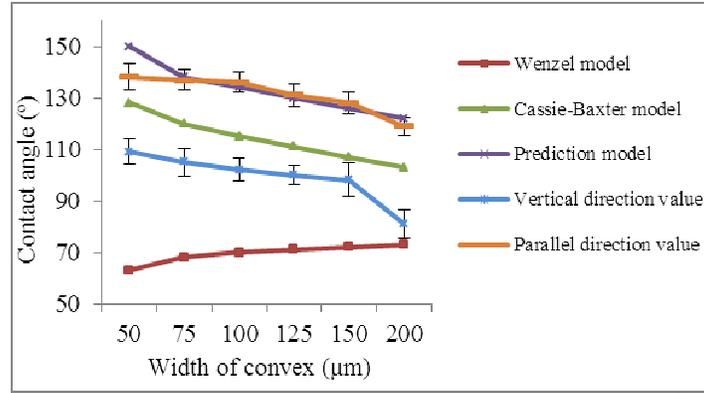Table 3 Contact angle obtained through different methods for Ti6Al4V

Width of convex/μm	Wenzel model θ_W/°	Cassie-Baxter model θ_{CB}/°	Prediction model θ/°	Vertical direction θ/° ($\pm$SE)	Parallel direction θ/° ($\pm$SE)

50	50	126	142	104±5[a]	135±5[b]
75	58	118	131	100±6[a]	130±4[b]
100	61	113	127	97±4[a]	126±3[b]
125	63	108	123	95±3[a]	119±4[b]
150	64	104	120	90±7[a]	115±4[b]
200	66	100	116	77±6[a]	113±3[b]

SE represent standard error from the mean value of 6 replicates, different letters represent significant differences (p≤0.05).

From Table 2 and Table 3, it can be seen that the contact angle for Ti6Al4V is always smaller than that of PMMA workpiece. That is duo to the surface free energy of the workpiece Ti6Al4V used in experiments is larger than workpiece of PMMA [18]. The surface free energy can affect the value of Yong contact angle, which in turn affect the value of impact factor K. The larger the surface free energy, the smaller of Yong contact angle. According to the expression of K, the smaller Yong contact angle, corresponds to smaller K value and results in smaller predicted contact angle. The experimental results and calculated results are very nice illustrations of this point.

The contrast curves for obtained contact angles are shown in Fig. 12.

(a) Contrast curve for obtained contact angles for PMMA.

(b) Contrast curve for obtained contact angles for Ti6Al4V.

Fig. 12 Contrast curves for obtained contact angles for different materials with different methods. Error bars indicate SE

From Fig. 12, it can be seen that for both PMMA and Ti6Al4V materials, when the observation direction is parallel to the convex, the established prediction model can forecast the contact angle very well; when the observation direction is vertical to the convex, the Cassie-Baxter is better for predicting the contact angle. For both models, the value of contact angle decreases with increase of the convex width. The difference is mainly coming from two aspects: on the one hand, the chatter of the machine tool makes their exit difference between the design sizes and dimensioning size which can change the contact angle; on the other hand, for the material's plasticity, the machined surface roughness is large which can increase the chance of forming composite contact, and consequently the actually contact angle can be different.

The trend of Fig. 12 agrees with the results form by Li, Fang and Rahman, who also used free energy analytical methods [19-21]. The difference is that the energy model established in this paper calculates the absolute value of energy, while the other three models can only calculate relative values. The absolute value of energy can not only be used to calculate the change of energy under same micro-structured surface, but also can calculate the change of energy under different micro-structured surface which is not provided by other models.

According to the above analysis, the established model can predict the contact angle accurately. When a solvent other than water were used as tested liquid, according to the expression of impact factor K, the bigger the surface tension is, the greater of the Yong contact angle, the bigger of the contact angle will be predicted and measured which agrees with the results form by Gindl [22].

5. Conclusions

A contact angle prediction model based on Gibbs free energy was established in this paper. It considers the effects of unilateral force and area constraints. The solid-liquid, solid-vapor and liquid-vapor contact length were calculated through geometric analysis respectively. The flowing conclusions can be obtained:

1. The effects of micro-structured surface parameters on contact angle were investigated. Results indicated that the contact angle could be increased by increasing concave depth or reducing convex height.

2. Micro-machining experimental results revealed that the established prediction model could estimate the contact angle very well when the observed direction is parallel to the convex of the machined micro-structured surface.

3. The workpiece surface free energy can affect the value of Yong contact angle, which in turn affect the value of impact factor. The larger the surface free energy, the smaller Yong contact angle, corresponding to smaller predicted and measured contact angle.

ACKNOWLEDGEMENT

REFERENCES

[1] B. Dean, B. Bhushan, Shark-skin surfaces for fluid-drag reduction in turbulent flow: a review, Phlos. T. Roy. Soc. A. 368 (2010) 4775-4806.

[2] T. Sun, G. Wang, L. Feng, B. Liu, Y. Ma, L. Jiang, D. Zhu, Reversible switching between superhydrophilicity and superhydrophobicity, Angew. Chem. Int. Edit. 43 (2004) 357-360.

[3] T. Sun, H. Tan, D. Han, Q. Fu, L. Jiang, No platelet can adhere—largely improved blood compatibility on nanostructured superhydrophobic surfaces, Small. 1 (2005) 959-963.

[4] R. Blossey, Self-cleaning surfaces-virtual realities, Nat. Mater. 2 (2003) 301-306.

[5] C. Neinhuis, W. Barthlott, Characterization and distribution of water-repellent, self-cleaning plant surfaces, Ann. Bot. London. 79 (1997) 667-677.

[6] A. Marmur, Wetting on hydrophobic rough surfaces: To be heterogeneous or not to be, Langmuir. 19 (2003) 8343-8348.

[7] T. Young, An essay on the cohesion of fluids, Philosoph. Trans. Royal. Soc. London. 95 (1805) 65-87.

[8] R.N. Wenzel, Resistance of solid surfaces to wetting by water, Ind. Eng. Chem. Res. 28(8)(1936) 988-994.

[9] A.B.D. Cassie, S. Baxter, Wettability of porous surfaces, Trans. Faraday. Soc. 40(1944) 546-551.

[10] Q.S. Zheng, Y. Yu, Z.H. Zhao, Effects of hydraulic pressure on the stability and transition of wetting modes of superhydrophobic surfaces, Langmuir. 21(26) (2005) 12207-12212.

[11] N.A. Patankar, On the modeling of hydrophobic contact angles on rough surfaces, Langmuir. 19(2003)1249-1253.

[12] R.E. Johnson, R.H. Dettre, Contact angle, wettability and adhesion, Washington DC, 1964.

[13] J.H. Song, M. Sakai, N. Yoshida, Dynamic hydrophobicity of water droplets on the line-patterned hydrophobic surfaces. Surf. Sci. 600(2006) 2711-2717.

[14] D. Song, B. Song, H. Hu, X. Du, Z. Ma, Contact angle and impinging process of droplets on partially grooved hydrophobic surfaces, Appl. Therm. Eng. 85 (2015) 356-364.

[15] Y.L. Wan, X.R. Zhang, L.X. Zhang, Z.J. Yu, Hydrophobic aluminum alloy surface fabricated by high speed micro-milling technology, China. Surf. Eng. 26 (5)(2013) 37-42.

[16] T. Nishino, M. Meguro, K. Nakamae, M. Matsushita, Y. Ueda, The lowest surface free energy based on-CF3 alignment, Langmuir. 15(13)(1999) 4321-4323.

[17] W. Li, G. Fang, Y. Li, G. Qiao, Anisotropic wetting behavior arising from superhydrophobic surfaces: parallel grooved structure, J. Phys. Chem. B. 112 (24) (2008) 7234-7243.

[18] J.M. Schuster, C.E. Schvezov, M.R. Rosenberger, Analysis of the results of surface free energy measurement of Ti6Al4V by different methods, Procedia. Mater. Sci. 8(2015)732-741.

[19] W. Li, A. Amirfazli, A thermodynamic approach for determining the contact angle hysteresis for super-hydrophobic surfaces, J. Colloid. Interf. Sci. 292 (1) (2005) 195-201.

[20] G. Fang, W. Li, X. Wang, Droplet motion on designed micro textured super-hydrophobic surfaces with tunable wettability, Langmuir. 24 (20) (2008) 11651-11660.

[21] M.A. Rahman, A.M. Jacobi, Wetting behavior and drainage of water droplets on microgrooved brass surfaces, Langmuir. 28(37) (2012) 13441-13451.

[22] M. Gindl, G. Sinn, W. Gindl, A. Reiterer, S. Tschegg, A comparison of different methods to calculate the surface free energy of wood using contact angle measurements, Colloids. Surf. A Physicochem. Eng. Asp. 181(2001)279-287.
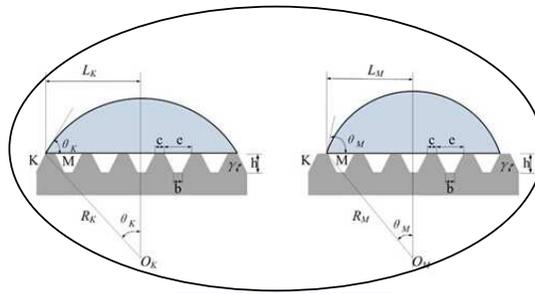
Highlights

1. The research built prediction model of contact angle based on minimum Gibbs free energy, the effects of unilateral force, area constraints of the droplets and micro-structural parameters of the interfaces are introduced.
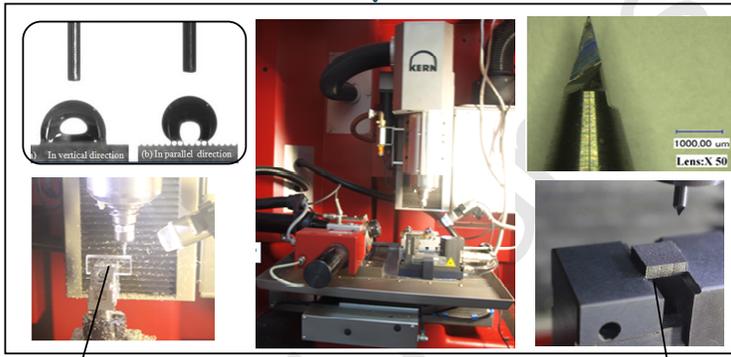
2. Micro-milling experiments have been conducted to fabricate the hydrophobic surface to validate the predictive capability of the contact angle model.

3. Our findings may have general implications in the optimization of hydrophobic structure parameters and will lead to methodologies for cost-effective monitoring and control of surface hydrophobic properties.
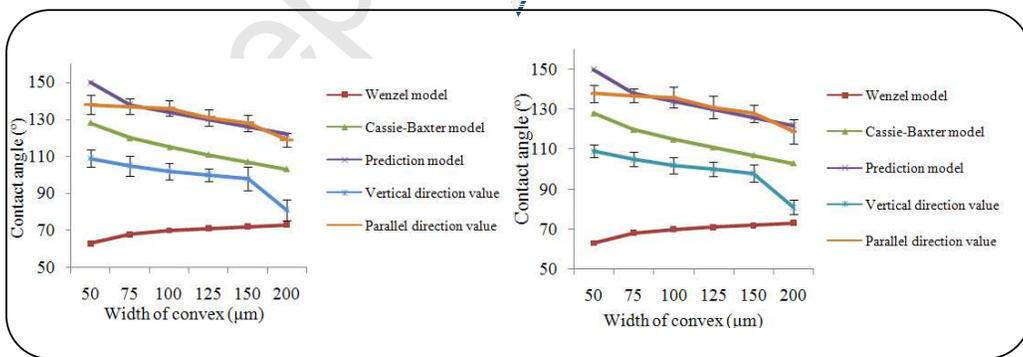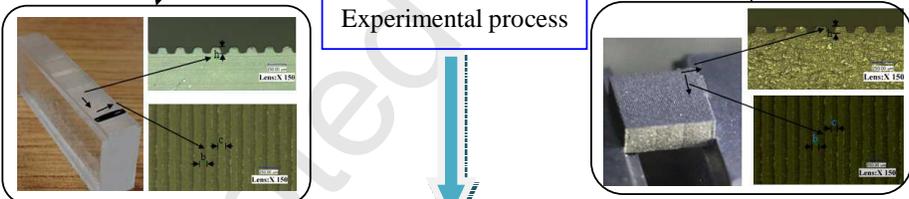
Theoretical basis

Experimental process

Results